The Astrophysical Journal Letters, 895:L47 (8pp), 2020 June 1 https://doi.org/10.3847/2041-8213/ab93d7
© 2020. The American Astronomical Society. All rights reserved.

Super-Rayleigh Slopes in Transmission Spectra of Exoplanets Generated by Photochemical Haze

Kazumasa Ohno[1] and Yui Kawashima[2]
[1] Department of Earth and Planetary Sciences, Tokyo Institute of Technology, Meguro, Tokyo, 152-8551, Japan; ohno.k.ab@eps.sci.titech.ac.jp
[2] SRON Netherlands Institute for Space Research, Sorbonnelaan 2, 3584 CA Utrecht, The Netherlands
Received 2020 March 16; revised 2020 May 15; accepted 2020 May 18; published 2020 June 4

Abstract

Spectral slopes in optical transmission spectra of exoplanetary atmospheres encapsulate information on the properties of exotic clouds. The slope is usually attributed to the Rayleigh scattering caused by tiny aerosol particles, whereas recent retrieval studies have suggested that the slopes are often steeper than the canonical Rayleigh slopes. Here, we propose that photochemical haze formed in vigorously mixing atmospheres can explain such super-Rayleigh slopes. We first analytically show that the spectral slope can be steepened by the vertical opacity gradient in which atmospheric opacity increases with altitude. Using a microphysical model, we demonstrate that such an opacity gradient can be naturally generated by photochemical haze, especially when the eddy mixing is substantially efficient. The transmission spectra of hazy atmospheres can be demarcated into four typical regimes in terms of the haze mass flux and eddy diffusion coefficient. We find that the transmission spectrum can have a spectral slope 2–4 times steeper than the Rayleigh slope if the eddy diffusion coefficient is sufficiently high and the haze mass flux falls into a moderate value. Based on the eddy diffusion coefficient suggested by a recent study of atmospheric circulations, we suggest that photochemical haze preferentially generates super-Rayleigh slopes at planets with equilibrium temperatures of 1000–1500 K, which might be consistent with results of recent retrieval studies. Our results would help interpret the observations of spectral slopes from the perspective of haze formation.

Unified Astronomy Thesaurus concepts: Exoplanet atmospheres (487); Hot Jupiters (753); Optical observation (1169); Transmission spectroscopy (2133)

1. Introduction

Transmission spectroscopy is a powerful way to explore the properties of exoplanetary atmospheres (e.g., Charbonneau et al. 2002; Pont et al. 2013; Kreidberg et al. 2014; Sing et al. 2016). One of the remarkable features of the transmission spectra is the rise of transit depth toward blue in the optical wavelength, called a spectral slope. The slope is quantified by (e.g., Lecavelier Des Etangs et al. 2008)

$$\frac{dR_{\rm p}}{d\ln\lambda} = H\alpha, \tag{1}$$

where $R_{\rm p}$ is the planetary radius, λ is the wavelength, H is the pressure scale height, and α is the spectral index of atmospheric opacity, i.e., $\kappa \propto \lambda^{\alpha}$. Utilizing Equation (1), measurements of the slopes can help to constrain atmospheric properties as well as the properties of exoplanetary clouds.

The spectral slopes are often attributed to the Rayleigh scattering ($\alpha = -4$) caused by tiny aerosols; however, several exoplanets actually exhibit the slopes steeper than the Rayleigh slope. Retrieval studies of Pinhas et al. (2019) and Welbanks et al. (2019) obtained the median spectral index of $\alpha \lesssim -5$ for most of the transmission spectra of hot Jupiters collected by Sing et al. (2016). For a more extreme example, Sedaghati et al. (2017) showed that the slope of a hot Jupiter WASP-19b is characterized by $\alpha = -26$. May et al. (2020) found an even steeper spectral slope of $\alpha \approx -35$ for a hot Neptune HATS-8b.

Several mechanisms potentially explain such super-Rayleigh slopes (SRSs hereafter). For example, unocculted star spots produce steep slope-like features in transmission spectra (e.g., McCullough et al. 2014) and potentially explain some SRSs. In fact, Espinoza et al. (2019) reported that the effects of star spots can explain the SRS of WASP-19b observed by Sedaghati et al. (2017). The mercapto radical, SH, can also yield a steep slope-like feature; though, it is responsible only for near the NUV wavelength ($\lambda \lesssim 0.46\ \mu$m, Zahnle et al. 2009b; Evans et al. 2018). Alternatively, tiny sulfide condensates, such as MnS, can produce slope-like features with $\alpha < -5$ (Pinhas & Madhusudhan 2017). Most recently, Kawashima & Ikoma (2019) found that photochemical haze can steepen the Rayleigh slope if atmospheric eddy diffusion is efficient.

In this study, we generalize the conditions in which photochemical haze produces the steep spectral slopes. In Section 2, we analytically show that the vertical opacity gradient can steepen the spectral slope more than the canonical Rayleigh slope. We also demonstrate that photochemical haze can generate such an opacity gradient. In Section 3, we calculate the synthetic transmission spectra of hazy atmospheres for a wide range of eddy diffusion coefficient and haze mass flux, and discuss the conditions of these parameters for which the SRSs emerge. In Section 4, we summarize our findings.

2. A Mechanism Producing Steep Spectral Slopes by Haze

A key factor producing the SRSs is the vertical gradient of atmospheric opacity. This fact is not captured by Equation (1), which was derived under the assumption of vertically uniform opacity. To examine the effect of vertical opacity gradient, we assume the opacity following $\kappa = \kappa_0(\lambda/\lambda_0)^{\alpha}(P/P_0)^{-\beta}$, where P is the atmospheric pressure and κ_0 is the opacity at the pressure level of P_0 and the wavelength of λ_0. Assuming hydrostatic equilibrium, and constant temperature and gravity throughout the atmosphere, the chord optical depth at the impact parameter of r is

calculated as (e.g., Benneke & Seager 2012)

$$\tau_{\rm v}(r) = 2\rho_{\rm g}(r)\kappa(r)\int_r^\infty \exp\left[-(1-\beta)\frac{r'-r}{H}\right]\frac{r'dr'}{\sqrt{r'^2-r^2}}, \tag{2}$$

where $\rho_{\rm g}$ is the atmospheric density, and r' is the radial distance from the center of the planet. Applying the transformation of $x = \sqrt{r^2 - r'^2}$ and approximation of $r' - r \approx x^2/2r$ as in Fortney (2005), Equation (2) is rewritten as

$$\tau_{\rm v}(r) = \rho_{\rm g}(r)\kappa(r)\int_{-\infty}^{\infty} \exp\left[-\frac{(1-\beta)x^2}{2rH}\right]dx. \tag{3}$$

Equation (3) diverges for $\beta \geqslant 1$, and thus a finite region of the atmosphere, in which the opacity source exists, should be taken into account for $\beta \geqslant 1$. Here, we see the solution of Equation (3) only for $\beta < 1$. As shown later, the opacity gradient produced by photochemical haze is mostly characterized by $\beta < 1$. For $\beta < 1$, the chord optical depth is calculated as

$$\tau_{\rm v}(r) = \rho_0\kappa_0\left(\frac{\lambda}{\lambda_0}\right)^\alpha\sqrt{\frac{2\pi R_0 H}{1-\beta}}\exp\left[-(1-\beta)\frac{r-R_0}{H}\right], \tag{4}$$

where ρ_0 is the atmospheric density at the reference radius of R_0. The observed planetary radius is corresponding to the radius at $\tau_{\rm v} \sim 1$. Inserting $\tau_{\rm v} = 1$ in Equation (4), the observed radius is given by

$$R_{\rm p} = R_0 + \frac{H}{1-\beta}\ln\left[\rho_0\kappa_0\left(\frac{\lambda}{\lambda_0}\right)^\alpha\sqrt{\frac{2\pi R_0 H}{1-\beta}}\right]. \tag{5}$$

Differentiating Equation (5) with respect to λ, we achieve a spectral slope with vertical opacity gradient applicable for $\beta < 1$:

$$\frac{dR_{\rm p}}{d\ln\lambda} = \frac{H\alpha}{1-\beta}. \tag{6}$$

Equation (6) is essentially the same as Equation (1) except for the factor of $(1-\beta)^{-1}$.

An important implication of Equation (6) is that the spectral index α (or scale height H) is degenerated with vertical opacity gradient β. Notably, for $0 < \beta < 1$ in which the opacity is higher at higher altitude, the slope is steepened by a factor of $(1-\beta)^{-1}$ from the classical prediction of Equation (1). Indeed, a recent retrieval study of Zhang et al. (2020) suggested that aerosols are more abundant in the upper atmosphere in hot Jupiter HD189733b that exhibits the SRS, consistent with the theory presented here. Thus, it is crucial to take into account the vertical opacity gradient to explore the nature of SRSs.

The remaining question is what causes the opacity gradient with $0 < \beta < 1$. We suggest that photochemical haze can naturally produce such a gradient. As shown in the Appendix, for haze particles much smaller than the gas mean free path and the relevant wavelength, the opacity can be written as

$$\kappa = \frac{36\pi gHF}{\rho_{\rm p}}\underbrace{\frac{1}{Pv_{\rm t}}\left[1-\exp\left(-\frac{v_{\rm t}H}{K_{\rm z}}\right)\right]}_{\text{Pressure dependence}}\underbrace{\frac{nk\lambda^{-1}}{(n^2-k^2+2)^2+(2nk)^2}}_{\text{Wavelength dependence}}, \tag{7}$$

where F is the haze mass flux, $K_{\rm z}$ is the eddy diffusion coefficient, g is the surface gravity, $\rho_{\rm p}$ is the particle density, and n and k are the real and imaginary parts of the complex refractive index. $v_{\rm t}$ is the terminal velocity of haze particles approximated by (Woitke & Helling 2003)

$$v_{\rm t} \approx \frac{\rho_{\rm p} g^2 H}{P\sqrt{8k_{\rm B}T/\pi m_{\rm g}}}a, \tag{8}$$

where $k_{\rm B}$ is the Boltzmann constant, T is the temperature, $m_{\rm g}$ is the mean mass of atmospheric gas particles, and a is the particle radius. The asymptotic behaviors of Equation (7) clarify the pressure dependence as

$$\kappa \propto \begin{cases} P^{-1} & (v_{\rm t}H/K_{\rm z} \ll 1) \\ a^{-1}\rho_{\rm p}^{-1} & (v_{\rm t}H/K_{\rm z} \gg 1). \end{cases} \tag{9}$$

Haze produces the vertical gradient with $\beta = 1$ when eddy diffusion dominates over the settling. Thus, strong eddy diffusion acts to steepen the spectral slope. When the settling is dominant, the gradient depends on how particle sizes and densities vary with altitude. In the next section, we numerically investigate the haze-produced spectral slopes using a microphysical model.

3. Numerical Investigations of Haze-produced Spectral Slopes

3.1. Method

We conduct a series of calculations for haze particle growth and synthetic transmission spectra. We utilize a two-moment microphysical model of Ohno & Okuzumi (2018) that takes into account the eddy diffusion, gravitational settling, and particle growth. The moment model suffices to examine whether haze can produce SRSs, as the model can capture the basic effects of haze formation on transmission spectra (Kawashima & Ikoma 2018). We assume spherical particles with constant density of 1 g cm^{-3} and ignore the condensation of mineral vapors for the sake of simplicity. The monomer production profile is prescribed by a log-normal profile given by (Ormel & Min 2019)

$$\dot{\rho}_{\rm haze} = \rho_{\rm g} g\frac{F}{\sigma P\sqrt{2\pi}}\exp\left[-\frac{1}{2\sigma^2}\left(\ln\frac{P}{P_*}\right)^2\right], \tag{10}$$

where the characteristic height of monomer production P_* and the width of the distribution σ are set to $P_* = 10^{-6}$ bar and $\sigma = 0.5$ to mimic the profile predicted by photochemical models (e.g., Kawashima & Ikoma 2019). Correspondingly, we include the increase of a particle number density as $\dot{n}_{\rm haze} = 3\dot{\rho}_{\rm haze}/4\pi a_0^3\rho_{\rm p}$, where a_0 is the monomer radius and assumed to be $a_0 = 1$ nm. The pressure-temperature structure for a solar composition atmosphere is constructed by an analytical model of Guillot (2010) using the same parameters adopted in Kawashima & Ikoma (2019) for their case of irradiation temperature of 790 K.[3]

We compute synthetic transmission spectra of hazy atmospheres using the model of Ohno et al. (2020) assuming the planetary mass of GJ 1214b ($6.26M_{\rm Earth}$, Anglada-Escudé et al. 2013) and the reference radius of $R_0 = 2.35R_{\rm Earth}$ at $P = 10$ bar.

[3] The temperature is a product of $\sqrt{2}$ and equilibrium temperature, which characterizes irradiation intensity (see, e.g., Guillot 2010).

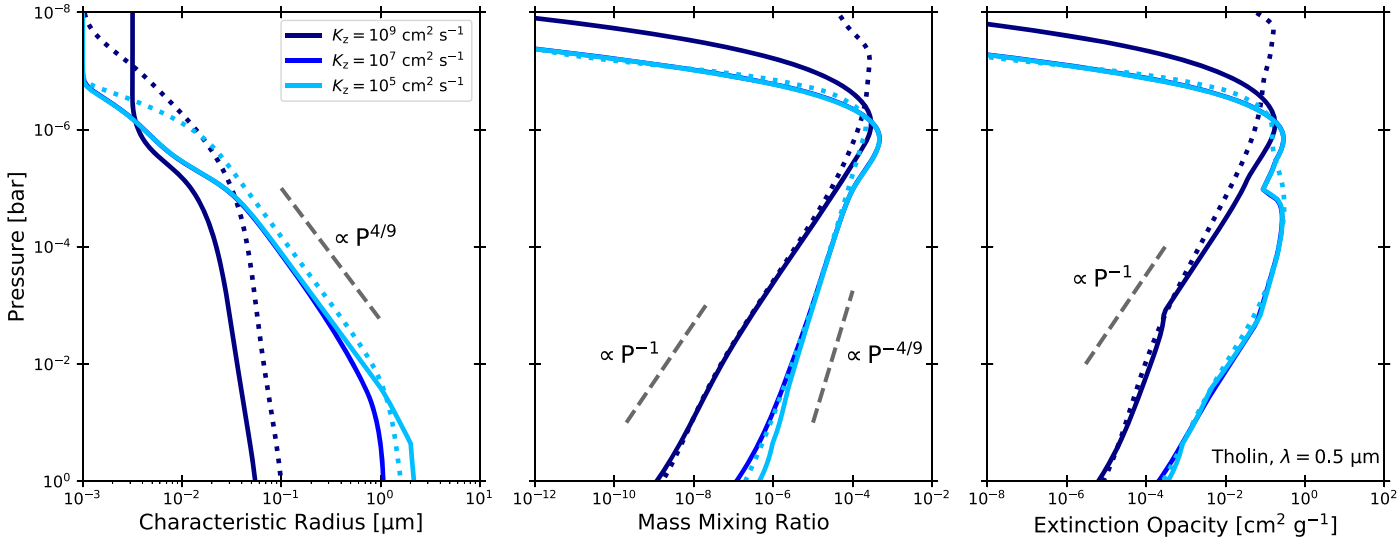

Figure 1. Vertical haze distributions for different eddy diffusion coefficients. From left to right, each column shows the vertical distributions of the characteristic particle size, the haze mass mixing ratio, and the extinction opacity for the tholin optical constants at $\lambda = 0.5\ \mu$m, respectively. Different colored lines show the distributions for different K_z with haze mass flux $F = 10^{-12}$ g cm^{-2} s^{-1}. Dotted lines denote the distributions of a volume-weighted particle size predicted by a bin scheme for $K_z = 10^5$ and 10^9 cm^2 s^{-1} taken from Figure 17 of Kawashima & Ikoma (2019), where the column-integrated photolysis rate of haze precursors is $\sim 10^{-12}$ g cm^2 s^{-1} (see their Table 1).

We introduce a metric quantifying steepness of the spectral slopes defined as (Pinhas & Madhusudhan 2017)

$$\mathcal{S} \equiv \frac{1}{H}\frac{dR_p}{d\ln\lambda}. \tag{11}$$

We use the U band ($\lambda = 365$ nm, FWHM of 66 nm) and V band ($\lambda = 551$ nm, FWHM of 88 nm) (Binney & Merrifield 1998) to calculate $\mathcal{S}$, similar to Pinhas & Madhusudhan (2017). The haze opacity is calculated by the BHMIE (Bohren & Huffman 1983), assuming spherical particles. The refractive index is unknown for exoplanetary haze. We test the two representative refractive indices; a Titan haze analog (tholin, Khare et al. 1984) and a complex refractory hydrocarbon (soot) compiled by Lavvas & Koskinen (2017).

3.2. Haze Vertical Profiles

Haze vertical distributions substantially vary with altitude, as suggested by previous studies (e.g., Lavvas & Koskinen 2017; Kawashima & Ikoma 2018, 2019; Adams et al. 2019; Kawashima et al. 2019; Lavvas et al. 2019; Gao & Zhang 2020). Figure 1 shows the vertical distributions of haze characteristic size and mass mixing ratio for $F = 10^{-12}$ g cm^{-2} s^{-1} and different K_z. We have confirmed that our two-moment model well reproduces the distributions simulated by the bin scheme (dotted lines) taken from Kawashima & Ikoma (2019). In principle, the particle size increases with decreasing altitude because of collisional growth. The higher the eddy diffusion coefficient is, the smaller the particle size is. This is because efficient vertical mixing transports the particles downward before they grow into large sizes (Kawashima & Ikoma 2019). The high eddy diffusion coefficient also produces a steep vertical gradient in the mass mixing ratio, as seen in the case of $K_z = 10^9$ cm^2 s^{-1}. This results in the steep vertical opacity gradient, as predicted in Section 2.

The vertical opacity gradient also appears when the settling dominates over the eddy diffusion, as seen in the cases of $K_z = 10^7$ and 10^5 cm^2 s^{-1}. This is because the particle size is larger in the deeper atmosphere due to collisional growth, leading to yield vertical gradient in the mass mixing ratio. The vertical distributions can be further understood from a timescale argument. The particle can grow until the settling timescale, $\tau_{\rm settl} = H/v_t$, becomes shorter than the collisional timescale. For particles smaller than the gas mean free path, the collision timescale is approximated by (e.g., Rossow 1978)

$$\tau_{\rm coll} \approx \frac{1}{4}\sqrt{\frac{\rho_p}{3ak_BT}}\frac{m_{\rm haze}}{\rho_{\rm haze}} = \frac{1}{4}\sqrt{\frac{\rho_p}{3ak_BT}}\frac{m_{\rm haze}v_t}{F}, \tag{12}$$

where we have invoked the mass conservation $\rho_{\rm haze}v_t = F$. Solving $\tau_{\rm coll} = \tau_{\rm sett}$ with Equation (8), the size is estimated as

$$a = \left(\frac{24FP^2}{\pi^2\rho_p^3 g^3}\sqrt{\frac{3k_BT}{\rho_p}}\right)^{2/9}. \tag{13}$$

Equation (13) indicates that the particle size is proportional to $P^{4/9}$, which is indeed seen in Figure 1. Therefore, the mass mixing ratio is proportional to $P^{-4/9}$ for small K_z regimes (see Equations (8) and (A2)), resulting in the opacity being higher at higher altitude. In summary, the haze opacity is higher at higher altitude for all K_z.

3.3. Transmission Spectra

The haze steepens the spectral slope for high K_z, as found by Kawashima & Ikoma (2019). The top panel of Figure 2 shows the synthetic transmission spectra for various K_z assuming the tholin optical constants. For the tcase of $K_z = 10^9$ cm^2 s^{-1}, haze produces the spectral slope characterized by $\mathcal{S} \approx -12$ in the optical wavelength, quite steeper than the canonical Rayleigh slope ($\mathcal{S} = -4$). This stems from the vertical mass gradient produced by efficient eddy diffusion (Section 3.2). The spectra for $K_z = 10^7$ and 10^5 cm^2 s^{-1} nearly superpose each other, as the vertical distributions are nearly the same.

The haze steepens the spectral slope only when the mass flux falls into a moderate value. As shown in the middle panel of Figure 2, the steep slope disappears in both cases of high- and

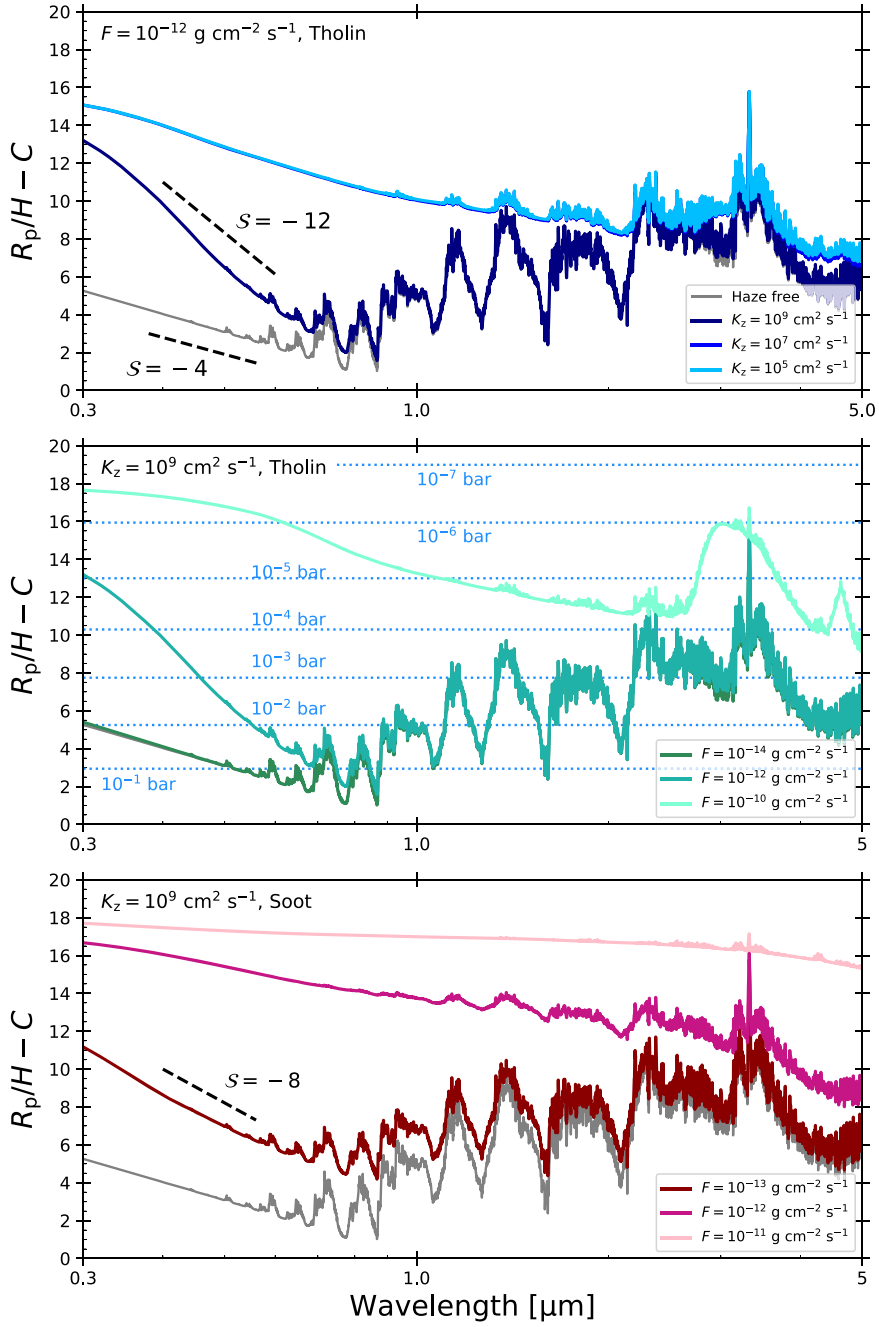

Figure 2. Synthetic transmission spectra of hazy atmospheres. The vertical axis is the planetary radius normalized by the scale height of $H = 180$ km, the value for $P \sim 10^{-3}$ bar, with an offset. The top panel shows the spectra for different K_z with $F = 10^{-12}$ g cm^{-2} s^{-1}. The middle and bottom panels show the spectra for different F with $K_z = 10^9$ cm^{-2} s^{-1}. The tholin refractive index is assumed for the top and middle panels, while the soot refractive index is assumed for the bottom panel. Horizontal dotted lines in the middle panel denote the $R_p/H - C$ corresponding to the pressure levels from 10^{-1} to 10^{-7} bar.

low-mass flux. The low-mass flux ($F = 10^{-14}$ g cm^{-2} s^{-1}) leads to the production of a spectrum superposed on a haze-free spectrum because the haze becomes optically thin as compared to the Rayleigh scattering opacity of H_2. By contrast, the high-mass flux ($F = 10^{-10}$ g cm^{-2} s^{-1}) leads to a flatted spectrum because the haze becomes optically thick near the monomer formation region ($\sim 10^{-6}$ bar) up to a relatively long wavelength.

The spectral slope also depends on the optical constants. The bottom panel of Figure 2 shows the spectra calculated with the soot optical constants. The soot haze tends to flatten the spectra owing to the weak wavelength dependence of its absorption opacity. Although the slope is relatively gentle, the soot haze still produces the SRSs with $\mathcal{S} \approx -8$ for $K_z = 10^9$ cm^2 s^{-1} and $F = 10^{-11}$ g cm^{-2} s^{-1}.

3.4. In What Conditions Does Haze Produce SRSs?

There is a "sweet spot" in the F–K_z space to produce the SRSs. Figure 3 summarizes the spectral slopes calculated for U–V bands as a function of haze mass flux F and eddy diffusion coefficient K_z. The slopes are relatively flat (i.e., $\mathcal{S} \sim 0$) for very high F, as the haze becomes optically thick near the monomer formation region (Section 3.3). By contrast, low F and high K_z tend to yield

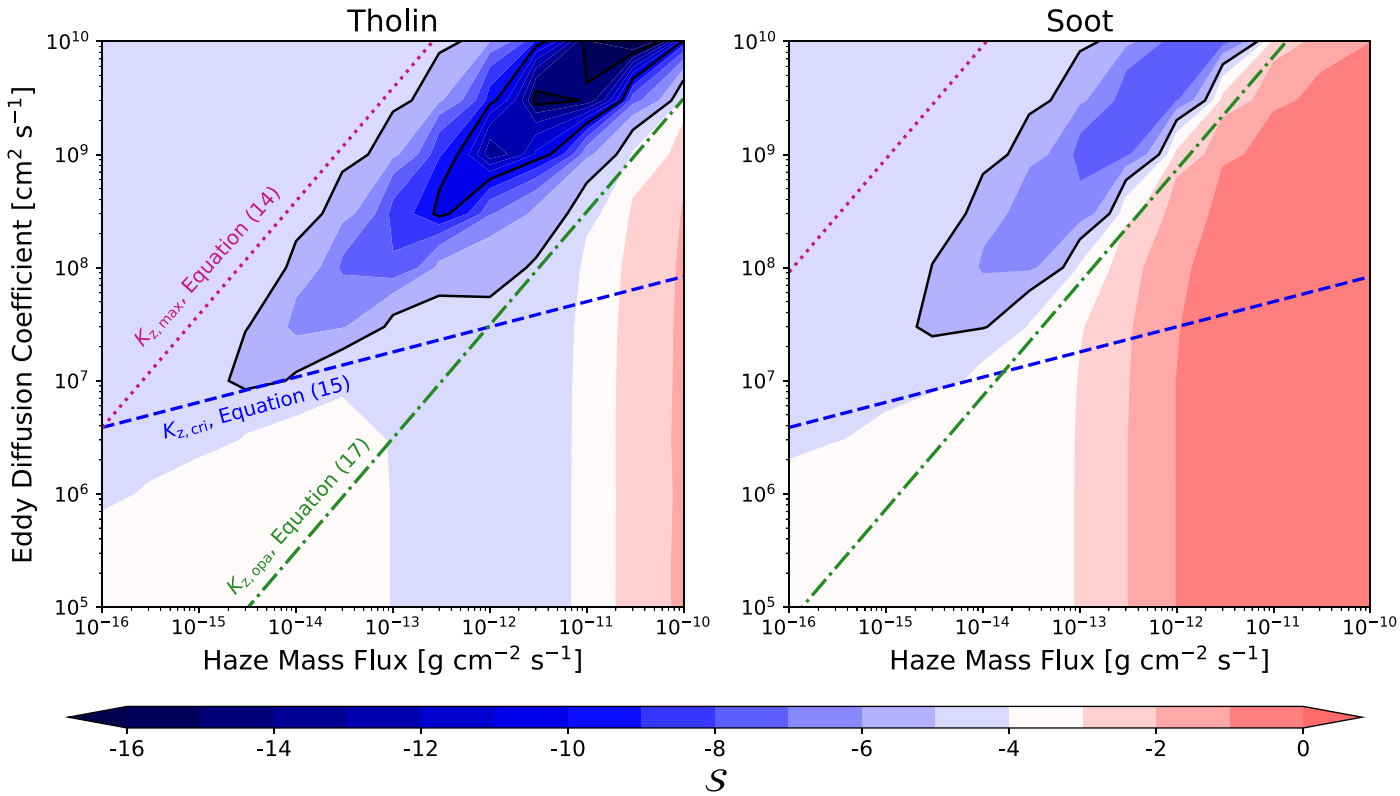

Figure 3. Gradient of the spectral slopes ($\mathcal{S}$, colorscale) as a function of eddy diffusion coefficient and haze mass flux. The left and right panels show the results for the tholin and soot haze, respectively. The black lines denote the contours of $\mathcal{S} = -5$, -10, and -15. The red dotted, blue dashed, and green broken lines denote Equations (14), (15), and (17), respectively, for $P = 1$ mbar and $\lambda = 0.55\ \mu$m. Here, we adopt the Rayleigh scattering cross section of a H_2 molecule, $\sigma_{gas} = 2.52 \times 10^{-28}\ \mathrm{cm}^2\ (\lambda/0.75\ \mu\mathrm{m})^{-4}$ (Lecavelier Des Etangs et al. 2008), to evaluate the gas opacity.

$\mathcal{S} = -4$, as the haze becomes optically thin. For moderate mass flux, say $F \gtrsim 10^{-14}\ \mathrm{g\ cm^{-2}\ s^{-1}}$, the slopes have $\mathcal{S} \sim -4$ for $K_z \lesssim 10^7\ \mathrm{cm^2\ s^{-1}}$ and $\mathcal{S} < -5$ for $K_z \gtrsim 10^7\ \mathrm{cm^2\ s^{-1}}$. The steep spectral slope (i.e., small $\mathcal{S}$) for high K_z stems from the steep vertical gradient in the mass mixing ratio (Section 3.2). In the parameter space examined here, the most steep slope has $\mathcal{S} \approx -16$ for the tholin haze and $\mathcal{S} \approx -8$ for the soot haze, which is found for $F \sim 10^{-12}$–$10^{-11}\ \mathrm{g\ cm^{-2}\ s^{-1}}$ and $K_z \sim 10^{10}\ \mathrm{cm^2\ s^{-1}}$.

The transmission spectra of hazy atmospheres can be demarcated into four typical regimes as presented in Figure 4. When K_z is extremely high, the haze becomes optically thin as compared to gas opacity, resulting in a haze-free spectrum (regime I). Equating Equation (7) and the gas opacity κ_{gas} with $v_t H/K_z \ll 1$, the threshold K_z above which the regime I applies is given by

$$K_{z,max} = \frac{36\pi g H^2 F}{\rho_p \kappa_{gas} P} \frac{nk\lambda^{-1}}{(n^2 - k^2 + 2)^2 + (2nk)^2}. \quad (14)$$

For $K_z < K_{z,max}$, the spectrum is substantially affected by haze. The spectral slope is significantly enhanced by haze when the eddy diffusion dominates over the settling of haze particles (regime II). Conversely, the slope is only weakly enhanced if the settling dominates over the eddy diffusion (regime III). Solving $\tau_{diff} = \tau_{sett}$ with Equations (8) and (13), where $\tau_{diff} = H^2/K_z$ is the diffusion timescale, the critical K_z above which eddy diffusion dominates over the settling is estimated as

$$\begin{aligned} K_{z,cri} &= \frac{\rho_p g^2 H^2}{P\sqrt{8gH/\pi}} \left(\frac{24FP^2}{\pi^2 \rho_p^3 g^3} \sqrt{\frac{3k_B T}{\rho_p}} \right)^{2/9} \\ &\sim 3 \times 10^7\ \mathrm{cm^2\ s^{-1}} \left(\frac{F}{10^{-12}\ \mathrm{g\ cm^2\ s^{-1}}} \right)^{2/9} \left(\frac{H}{200\ \mathrm{km}} \right)^{3/2} \\ &\quad \times \left(\frac{g}{10\ \mathrm{m\ s^{-2}}} \right)^{5/6} \left(\frac{P}{1\ \mathrm{mbar}} \right)^{-5/9} \left(\frac{T}{1000\ \mathrm{K}} \right)^{1/9} \\ &\quad \times \left(\frac{\rho_p}{1\ \mathrm{g\ cm^{-3}}} \right)^{2/9}. \end{aligned} \quad (15)$$

The spectrum eventually becomes flat when the mass flux is so high that haze is optically thick at the monomer formation region (regime IV). Since the vertical mass distribution does not follow a power law near the monomer formation region (see Figure 1), we crudely evaluate the optical depth as

$$\tau_s(P_*) \sim \frac{P_*}{gH} \kappa(P_*) \sqrt{2\pi R_p H}. \quad (16)$$

Inserting Equation (7) into (16) and solving $\tau_s(P_*) = 1$ with $v_t H/K_z \ll 1$, we achieve the threshold in terms of K_z as

$$K_{z,opa} = \frac{36\pi H F \sqrt{2\pi R_p H}}{\rho_p} \frac{nk\lambda^{-1}}{(n^2 - k^2 + 2)^2 + (2nk)^2}. \quad (17)$$

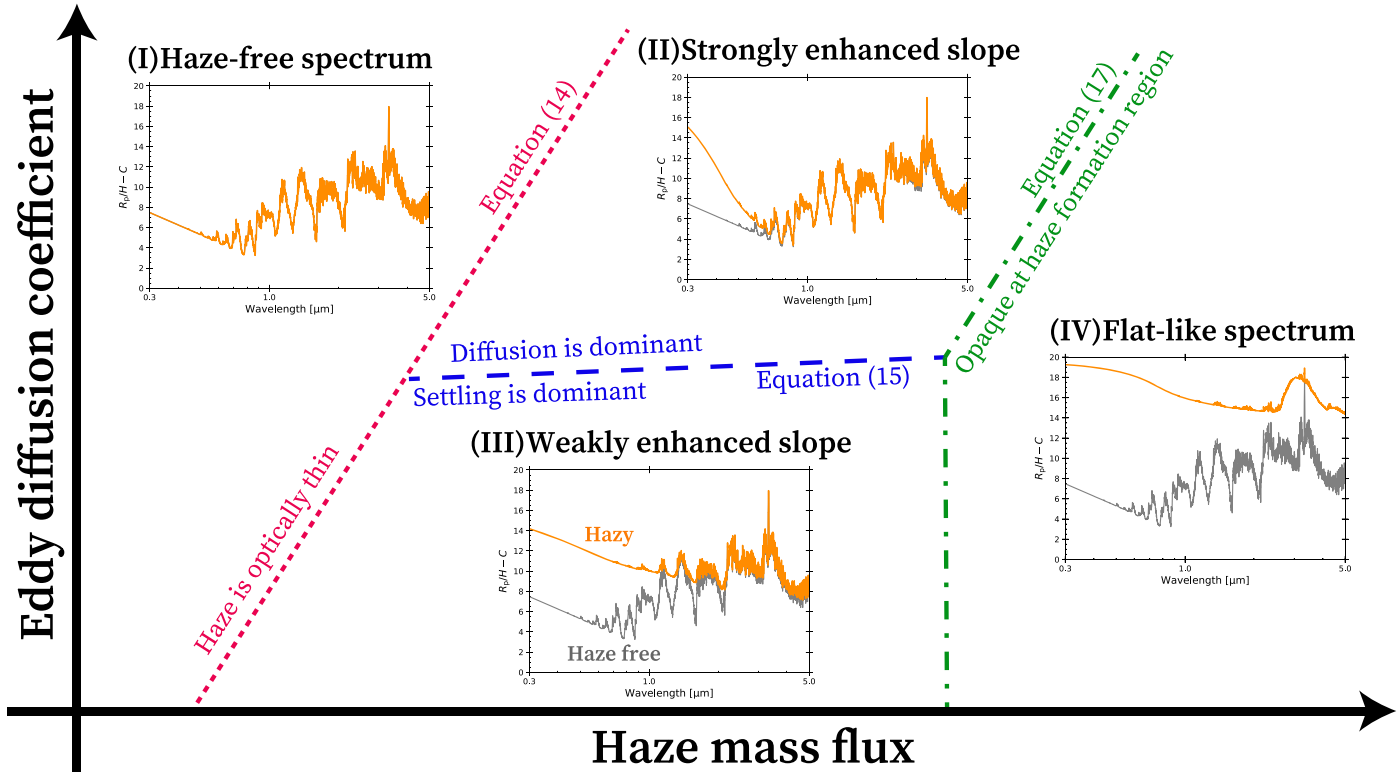

Figure 4. Transmission spectrum regimes in terms of haze mass flux and eddy diffusion coefficient (see Section 3.4). Each panel exhibits the typical shape of the transmission spectrum for hazy atmospheres (orange lines) compared to the haze-free spectrum (gray lines).

Equation (17) does not apply when the settling dominates over the eddy diffusion, i.e., $K_z < K_{z,\mathrm{cri}}$. Since the spectrum is invariant with K_z for the settling-dominated regime (see Figure 2), the threshold for $K_z < K_{z,\mathrm{cri}}$ is given as an intersection of Equations (15) and (17). We plot Equations (14), (15), and (17) in Figure 3 and find that the regime classification explains the basic behavior of spectral slopes. Notably, the SRSs preferentially emerge in regime II (see Figure 4), where the eddy diffusion coefficient falls into the sweet spot, namely $\max(K_{z,\mathrm{cri}}, K_{z,\mathrm{opa}}) < K_z < K_{z,\mathrm{max}}$. Alternatively, the SRSs emerge when the haze mass flux falls into a moderate value for given K_z; for example, $F \sim 10^{-13}$–10^{-11} g cm^{-2} s^{-1} for $K_z = 10^9$ cm^2 s^{-1} (see Figure 3). Thus, the SRSs might give a constraint on haze mass flux if the strength of eddy diffusion is well constrained.

4. Summary and Discussion

In this study, we have suggested that the super-Rayleigh slopes seen in transmission spectra of some exoplanets can be produced by photochemical haze. We have analytically shown that the spectral slope is steepened by the vertical gradient of atmospheric opacity, which is naturally generated by haze (Section 2). We have numerically confirmed that the haze can produce the spectral slope several times steeper than the canonical Rayleigh slope, especially when the eddy diffusion coefficient and the haze mass flux fall into the sweet spot (Section 3). We have also demarcated the transmission spectra of hazy atmospheres into four typical regimes (Figure 4). Our results would help to not only interpret the SRSs but also figure out how haze affects the transmission spectra.

One of the possible approaches for testing our idea is to search for the absorption feature of haze itself. For instance, Titan tholin exhibits absorption features at 3.0, 4.6, and 6.3 μm (e.g., Khare et al. 1984; Imanaka et al. 2004). It may be worth investigating whether planets with SRSs show the features at these wavelength. The actual optical constants of exoplanetary hazes are unknown. Therefore, laboratory studies on exoplanetary haze analogs (e.g., He et al. 2018; Hörst et al. 2018; Moran et al. 2020) are important to examine what optical constants are more plausible for exoplanet environments. The reliable optical constants will also help to quantify the effects of hazes on the spectral slopes.

There may be a "sweet spot" for planetary equilibrium temperature in which haze preferentially causes the SRSs. This is because the equilibrium temperature is associated with K_z (Komacek et al. 2019). Figure 5 shows the spectral slope $\mathcal{S}$ as a function of K_z and corresponding equilibrium temperature, where we have assumed the following relation

$$\log_{10}(K_z\ (\mathrm{m}^2\ \mathrm{s}^{-1})) = 2.110\left(\frac{T_{\mathrm{eq}}}{1000\ \mathrm{K}}\right) + 1.855. \qquad (18)$$

This relation is obtained by a linear fit to K_z simulated by Komacek et al. (2019) for drag-free atmospheres with 0.01 μm passive tracers at $P = 1$ mbar (their Figure 8). Haze preferentially produces steep slopes at an equilibrium temperature of $\sim$1000–1500 K in which K_z falls into the regime II. Figure 5 also exhibits the slope retrieved by Welbanks et al. (2019; their γ). Interestingly, in the retrieval results, planets with equilibrium temperature of $\sim$1200–1400 K tend to exhibit steep spectral slopes, similar to the haze-generated SRSs. We do not claim that the result verifies the haze hypotheses since there are many

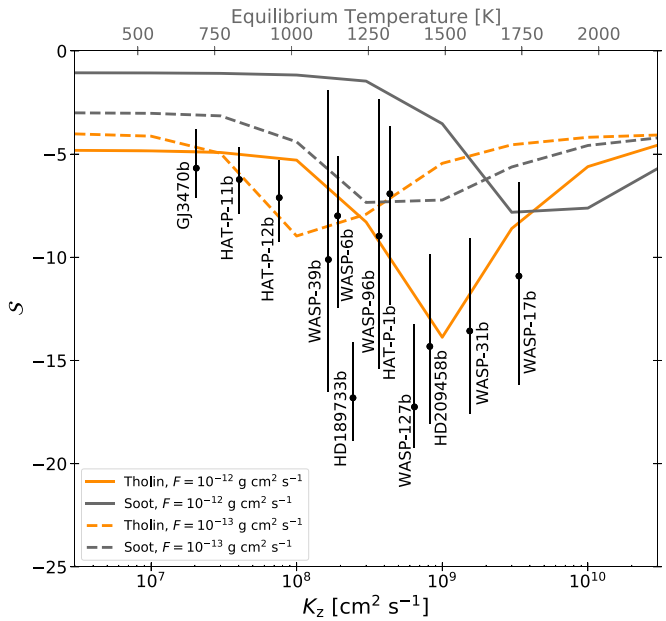

Figure 5. Haze-generated spectral slopes as a function of K_z. The solid and dashed lines show the slopes for $F = 10^{-12}$ and 10^{-13} g cm^2 s^{-1}, respectively, which are in line with the predictions from the column-integrated photolysis rate of hydrocarbons reported by previous studies (Lavvas & Koskinen 2017; Kawashima & Ikoma 2019). The orange and gray lines exhibit the slopes for tholin and soot haze, respectively. The black dots denote the slopes retrieved by Welbanks et al. (2019) with 1σ error bars.

uncertainties, such as stellar contamination (e.g., McCullough et al. 2014) and multidimension effects (e.g., Caldas et al. 2019; MacDonald et al. 2020), that should be assessed in the future. Rather, we suggest that measuring the spectral slopes for various equilibrium temperature can help to investigate whether the SRSs are predominantly caused by haze.

Photochemical haze also complements the model of mineral clouds. Current cloud microphysical models do not predict the optical spectral slope as steep as the Rayleigh slope (Gao & Benneke 2018; Lines et al. 2018; Lee et al. 2019; Powell et al. 2019; Ohno et al. 2020), except for Ormel & Min (2019) who showed some cases that succeeded in producing the steep spectral slopes. Although it has been believed that haze formation is inefficient in hot exoplanets where CH_4 is oxidized to CO (Zahnle et al. 2009a), recent laboratory studies suggest that CO also act as haze precursors (Hörst et al. 2018; He et al. 2019). Thus, haze may still be responsible for hot exoplanets that often show spectral slopes in their transmission spectra.

We thank Luis Welbanks for sharing retrieval results of Welbanks et al. (2019). We are also grateful to the anonymous referee for constructive comments that greatly improved the quality of this paper. K.O. is supported by JSPS KAKENHI grant Nos. JP18J14557 and JP19K03926. Y.K. is supported by the European Union's Horizon 2020 Research and Innovation Programme under Grant Agreement 776403.

Appendix
Derivation of Analytical Haze Opacity

In this appendix, we derive the vertical distribution of atmospheric opacity including haze. The steady vertical distribution of haze mass density $\rho_{\rm haze}$ is determined by the mass conservation, which reads

$$\frac{K_z}{gH^2}P^2\frac{\partial}{\partial P}\left(\frac{\rho_{\rm haze}}{\rho_{\rm g}}\right) - v_{\rm t}\rho_{\rm haze} = -F, \tag{A1}$$

where we have used the hydrostatic equilibrium, the ideal gas law, and the definition of H. In the upper atmospheres where haze particles are much smaller than gas mean free path, the terminal velocity can be approximated by Equation (8). For constant K_z, $\rho_{\rm p}$, and a, Equation (A1) is solved as

$$\frac{\rho_{\rm haze}}{\rho_{\rm g}} = \frac{gHF}{Pv_{\rm t}}\left[1 - \exp\left(-\frac{v_{\rm t}H}{K_z}\right)\right], \tag{A2}$$

where we have set the boundary condition of $\rho_{\rm haze} = 0$ at $P = \infty$. The extinction cross sections of haze particles may be approximated by absorption cross section, especially for particles much smaller than relevant wavelength. For such tiny particles, the absorption cross section is approximated by (Bohren & Huffman 1983; Kataoka et al. 2014)

$$\sigma_{\rm abs} \approx \pi a^2 \frac{24nk}{(n^2 - k^2 + 2)^2 + (2nk)^2}\frac{2\pi a}{\lambda}. \tag{A3}$$

Combining Equations (A2) and (A3), we finally achieve the opacity (Equation (7)) as

$$\kappa = \frac{3\sigma_{\rm abs}}{4\pi a^3\rho_{\rm p}}\frac{\rho_{\rm haze}}{\rho_{\rm g}} = \frac{36\pi gHF}{\rho_{\rm p}}\underbrace{\frac{1}{Pv_{\rm t}}\left[1 - \exp\left(-\frac{v_{\rm t}H}{K_z}\right)\right]}_{\text{Pressure dependence}}\underbrace{\frac{nk\lambda^{-1}}{(n^2 - k^2 + 2)^2 + (2nk)^2}}_{\text{Wavelength dependence}}, \tag{A4}$$

Equation (A4) demonstrates that, for tiny absorbing haze, the pressure dependence originated from the vertical mass gradient, while the wavelength dependence is from haze optical constants.

ORCID iDs

Kazumasa Ohno https://orcid.org/0000-0003-3290-6758
Yui Kawashima https://orcid.org/0000-0003-3800-7518

References

Adams, D., Gao, P., de Pater, I., & Morley, C. V. 2019, ApJ, 874, 61
Anglada-Escudé, G., Rojas-Ayala, B., Boss, A. P., Weinberger, A. J., & Lloyd, J. P. 2013, A&A, 551, A48
Benneke, B., & Seager, S. 2012, ApJ, 753, 100
Binney, J., & Merrifield, M. 1998, Galactic Astronomy (Princeton, NJ: Princeton Univ. Press)
Bohren, C. F., & Huffman, D. R. 1983, Absorption and Scattering of Light by Small Particles (New York: Wiley)
Caldas, A., Leconte, J., Selsis, F., et al. 2019, A&A, 623, A161
Charbonneau, D., Brown, T. M., Noyes, R. W., & Gilliland, R. L. 2002, ApJ, 568, 377
Espinoza, N., Rackham, B. V., Jordán, A., et al. 2019, MNRAS, 482, 2065
Evans, T. M., Sing, D. K., Goyal, J. M., et al. 2018, AJ, 156, 283
Fortney, J. J. 2005, MNRAS, 364, 649
Gao, P., & Benneke, B. 2018, ApJ, 863, 165

Gao, P., & Zhang, X. 2020, ApJ, 890, 93
Guillot, T. 2010, A&A, 520, A27
He, C., Hörst, S. M., Lewis, N. K., et al. 2018, ApJL, 856, L3
He, C., Hörst, S. M., Lewis, N. K., et al. 2019, ECS, 3, 39
Hörst, S. M., He, C., Lewis, N. K., et al. 2018, NatAs, 2, 303
Imanaka, H., Khare, B. N., Elsila, J. E., et al. 2004, Icar, 168, 344
Kataoka, A., Okuzumi, S., Tanaka, H., & Nomura, H. 2014, A&A, 568, A42
Kawashima, Y., Hu, R., & Ikoma, M. 2019, ApJL, 876, L5
Kawashima, Y., & Ikoma, M. 2018, ApJ, 853, 7
Kawashima, Y., & Ikoma, M. 2019, ApJ, 877, 109
Khare, B. N., Sagan, C., Arakawa, E. T., et al. 1984, Icar, 60, 127
Komacek, T. D., Showman, A. P., & Parmentier, V. 2019, ApJ, 881, 152
Kreidberg, L., Bean, J. L., Désert, J.-M., et al. 2014, Natur, 505, 69
Lavvas, P., & Koskinen, T. 2017, ApJ, 847, 32
Lavvas, P., Koskinen, T., Steinrueck, M. E., García Muñoz, A., & Showman, A. P. 2019, ApJ, 878, 118
Lecavelier Des Etangs, A., Pont, F., Vidal-Madjar, A., & Sing, D. 2008, A&A, 481, L83
Lee, G. K. H., Taylor, J., Grimm, S. L., et al. 2019, MNRAS, 487, 2082
Lines, S., Manners, J., Mayne, N. J., et al. 2018, MNRAS, 481, 194
MacDonald, R. J., Goyal, J. M., & Lewis, N. K. 2020, ApJL, 893, L43
May, E. M., Gardner, T., Rauscher, E., & Monnier, J. D. 2020, AJ, 159, 7
McCullough, P. R., Crouzet, N., Deming, D., & Madhusudhan, N. 2014, ApJ, 791, 55
Moran, S. E., Hörst, S. M., Vuitton, V., et al. 2020, arXiv:2004.13794
Ohno, K., & Okuzumi, S. 2018, ApJ, 859, 34
Ohno, K., Okuzumi, S., & Tazaki, R. 2020, ApJ, 891, 131
Ormel, C. W., & Min, M. 2019, A&A, 622, A121
Pinhas, A., & Madhusudhan, N. 2017, MNRAS, 471, 4355
Pinhas, A., Madhusudhan, N., Gandhi, S., & MacDonald, R. 2019, MNRAS, 482, 1485
Pont, F., Sing, D. K., Gibson, N. P., et al. 2013, MNRAS, 432, 2917
Powell, D., Louden, T., Kreidberg, L., et al. 2019, ApJ, 887, 170
Rossow, W. B. 1978, Icar, 36, 1
Sedaghati, E., Boffin, H. M. J., MacDonald, R. J., et al. 2017, Natur, 549, 238
Sing, D. K., Fortney, J. J., Nikolov, N., et al. 2016, Natur, 529, 59
Welbanks, L., Madhusudhan, N., Allard, N. F., et al. 2019, ApJL, 887, L20
Woitke, P., & Helling, C. 2003, A&A, 399, 297
Zahnle, K., Marley, M. S., & Fortney, J. J. 2009a, arXiv:0911.0728
Zahnle, K., Marley, M. S., Freedman, R. S., Lodders, K., & Fortney, J. J. 2009b, ApJL, 701, L20
Zhang, M., Chachan, Y., Kempton, E. M.-R., et al. 2020, arXiv:2004.09513